

Shallow penetrometer tests: theoretical and experimental modelling of penetration and dissipation stages¹

M.A. Schneider, S.A. Stanier, D.J. White, and M.F. Randolph

Abstract: Shallow penetrometers are devices that penetrate into and measure the properties of surficial offshore sediments via multi-phase tests involving penetration, dissipation, and rotation stages. In fine-grained soils such as silts and clays, these testing stages yield undrained strength, consolidation, and friction properties relevant to subsea pipeline and shallow foundation design. This paper describes toroid and hemiball devices of the scale for use in box-core samples and associated interpretation methods for the penetration and dissipation stages. The aim of the paper is to provide all tools needed to design and interpret these tests. New large-deformation finite element (LDFE) dissipation solutions are presented, which can be used for back-analysis of the dissipation stage. Results of an extensive laboratory proof testing exercise in kaolin clay, for both the hemiball and toroid penetrometers, are also reported. These results highlight the potential of the two devices to quickly and economically assess strength and consolidation characteristics of fine-grained sediments in box-core samples recovered to the deck of a site investigation vessel.

Key words: shallow penetrometer, offshore engineering, in situ testing, undrained penetration, dissipation.

Résumé : Les pénétrètres peu profonds sont des dispositifs qui pénètrent dans les sédiments superficiels en mer et mesurent leurs propriétés au moyen d'essais multiphasés comportant des étapes de pénétration, de dissipation et de rotation. Dans les sols à grain fin tels que les limons et les argiles, ces étapes d'essai donnent des propriétés de résistance, de consolidation et de frottement non drainées pertinentes pour la conception des conduites sous-marines et des fondations peu profondes. Cet article décrit les dispositifs toroïdaux et hémiballins de l'échelle à utiliser dans les échantillons de carottes de forage et les méthodes d'interprétation connexes pour les étapes de pénétration et de dissipation. L'objectif de cet article est de fournir tous les outils nécessaires à la conception et à l'interprétation de ces essais. De nouvelles solutions de dissipation par éléments finis à grande déformation (« LDFE ») sont présentées, qui peuvent être utilisées pour l'analyse rétrospective de l'étape de dissipation. Les résultats d'un vaste exercice d'essais en laboratoire dans l'argile kaolinique, tant pour l'hémiball que pour le pénétrètre toroïdal, sont également présentés. Ces résultats mettent en évidence le potentiel des deux dispositifs pour évaluer rapidement et économiquement la résistance et les caractéristiques de consolidation des sédiments à grain fin dans des carottes de forage récupérées sur le pont d'un navire de recherche sur le site. [Traduit par la Rédaction]

Mots-clés : pénétrètre peu profond, ingénierie en mer, essais in situ, pénétration non drainée, dissipation.

Introduction

Many offshore structures — such as pipelines and shallow foundations — rest on soft surficial marine clays. Reliable characterization of these top soil layers (often only half a metre) is key to developing robust and cost-effective designs for such infrastructure.

Conventional in situ testing procedures (e.g., cone penetrating test (CPT), T-bar or ball penetrometers) may be used to assess the shear strength profile of surficial soils (e.g., White et al. 2010a for the T-bar or Morton et al. 2014 for the ball penetrometer), although only very limited information about the interface friction properties can be gained with such testing methods. Recovering tube samples for laboratory testing (e.g., in situ coring of the seabed or recovering tube samples from a box-core sample on the deck of a survey vessel) is difficult, mainly because of sampling-

induced disturbance of such soft materials, which adversely affects element test results (Baligh et al. 1987; Clayton et al. 1998; Hover et al. 2013; Pineda et al. 2016). Additionally, element tests, in particular the interface shear box test (Westgate et al. 2018), should be representative of the conditions encountered offshore. At low effective normal stress levels ($\sigma'_n \sim 10$ kPa) relevant to subsea pipelines and shallow foundations, it is challenging to perform and interpret element tests due to spurious system friction generated by the apparatus. Corrections for these errors (e.g., Lehané and Liu 2013) become an increasingly large proportion of the measured overall system response as the effective normal stress levels reduce. The Cam-Tor apparatus (Kuo et al. 2015) and the tilt table (Pedersen et al. 2003) are two alternative testing techniques better suited to making measurements of drained interface friction at low stress levels. However, the sample recovery and transportation process, from an offshore testing site to an

Received 17 September 2018. Accepted 22 March 2019.

M.A. Schneider and M.F. Randolph. Centre for Offshore Foundation Systems, The University of Western Australia, Crawley, Australia.

S.A. Stanier.* Engineering Department, Cambridge University, Trumpington Street, Cambridge, CB2 1PZ, UK.

D.J. White. University of Southampton, University Road, Southampton, UK; Centre for Offshore Foundation Systems, The University of Western Australia, Crawley, Australia.

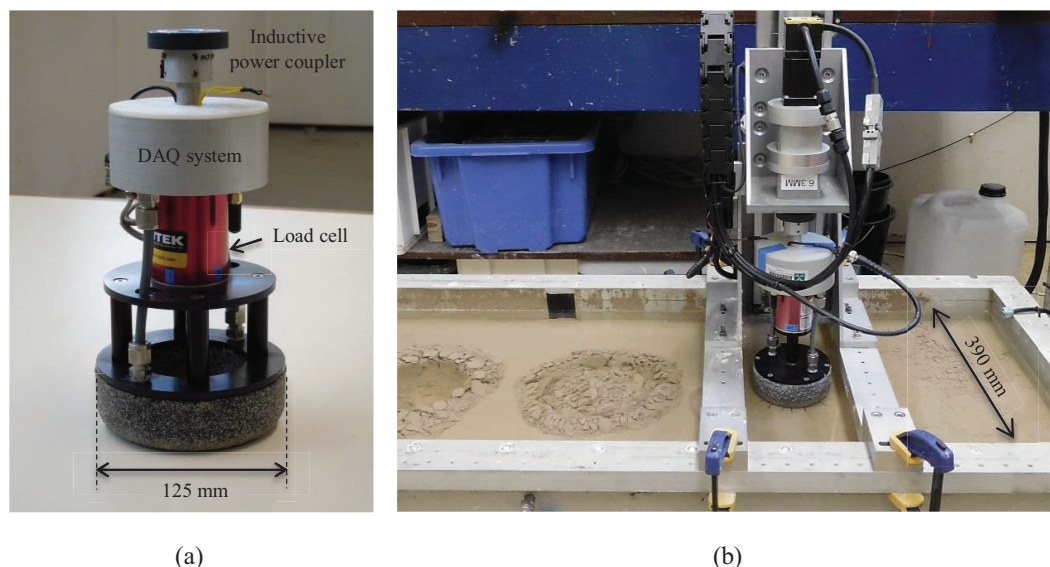
Corresponding author: Sam Stanier (email: sas229@cam.ac.uk).

*S.A. Stanier currently serves as an Editorial Board Member; peer review and editorial decisions regarding this manuscript were handled by C. Lake.

¹This paper is the first of two companion papers published in this issue (Schneider et al. 2020. Can. Geotech. J., 57. [dx.doi.org/10.1139/cgj-2018-0657](https://doi.org/10.1139/cgj-2018-0657)).

Copyright remains with the author(s) or their institution(s). Permission for reuse (free in most cases) can be obtained from [RightsLink](https://RightsLink.com).

Fig. 1. (a) Toroid penetrometer and (b) shallow penetrometer hemiball test. DAQ, data acquisition. [Colour online.]



onshore laboratory, leads to significant time delays and the risk of sample disturbance.

The toroid and hemiball penetrometers, two novel pipe-like investigation devices, have the potential to address these limitations (Yan et al. 2011a; Stanier and White 2015). They are capable of measuring near-surface soil properties in situ offshore at the seabed (deployed from either a frame or remotely operated vehicle (ROV)) or in a recovered box core (generally 0.5 m by 0.5 m in plan) on the deck of a survey vessel. A shallow penetrometer test is typically subdivided into penetration, dissipation, and rotation stages, targeting the strength, consolidation, and interface friction characteristics, respectively, of the underlying soil.

A major advantage of the shallow penetrometers is that the rotation stage of the tests may be interpreted using an effective stress approach, as pore-water pressures are monitored continuously via pressure transducers at various locations on the devices. In addition, there are two key advantages to the shallow penetrometer concept compared to the current “gold standard”, which is in situ model testing performed using systems such as the Fugro SMARTPIPE (White et al. 2010b); namely, that (i) continuous rotation effectively facilitates infinite sliding without the end effects associated with testing using an instrumented section of pipeline and (ii) the modest penetrometer diameters of box-core sized devices (25–100 mm) result in relatively short test durations, which allows the devices to be used “off the critical path” of operations during a geophysical or geotechnical survey.

The concept of the shallow penetrometer devices was first explored by Yan et al. (2011a, 2011b) via small-scale centrifuge tests and small-strain finite element (SSFE) simulations. Stanier and White (2015) investigated the initial undrained penetration stage in more detail and eventually developed an interpretation model, based on a series of comprehensive large-deformation finite element (LDFE) analyses. Following these initial studies, “box-core scale” versions of the penetrometers and a bespoke actuation system were manufactured at The University of Western Australia (see Fig. 1) as part of the Remote Intelligent Geotechnical Seabed Surveys Joint Industry Project (RIGSS JIP). Schneider et al. (2020a) provide a comprehensive description of the design of these box-core scale devices and associated system design considerations.

This paper and the accompanying companion paper (Schneider et al. 2020b) describe new interpretation methodologies for these box-core scale penetrometers and validate their operation in laboratory conditions. This paper illustrates the fundamentals of the penetration and dissipation phase, while the rotation stage is

outlined in the companion paper. The box core-scale hemiball has pore pressure sensors at the mid-face (45° from the invert) and so-called intermediate (22.5° from the invert) locations as illustrated in Fig. 2. New hemiball LDFE-dissipation solutions have been developed that can be used to interpret pore pressure measurements taken at any location on the surface of the device, allowing flexibility in the design of future versions of the device. A comprehensive laboratory testing program, for both the hemiball and the toroid penetrometers (more detailed information about these devices can be found in the next section), was conducted in kaolin clay samples. The test results demonstrate the potential of the shallow penetrometers to rapidly and consistently measure the strength and consolidation characteristics of the soft fine-grained sediments prevalent on the ocean floor in deep water locations.

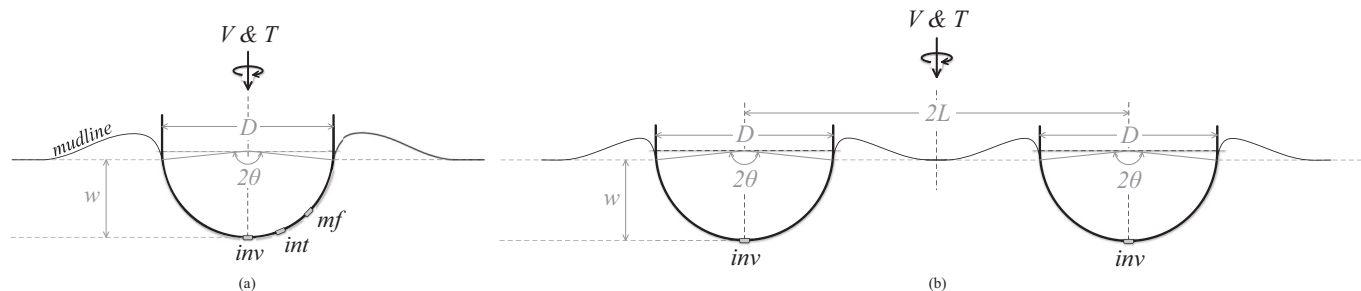
Shallow penetrometers

Hemiball and toroid penetrometers

Both hemiball and toroid penetrometers feature a curved underside that represents the shape of pipe-like infrastructure (e.g., seabed cables or pipelines), consequently minimizing uncertainties due to scaling for geometric effects (i.e., from planar interface properties measured in interface shear box tests to resistance on a curved pipeline). The device diameter, D , of the box-core sized penetrometers (Fig. 1) was selected as 100 and 25 mm for the hemiball and toroid, respectively. For the toroid (Fig. 2), an aspect ratio of $L/D = 2$, where L is the lever arm of the toroidal cylinder, was chosen to minimize adverse effects due to interference across the device (after Yan et al. 2011a).

Both penetrometers feature pore pressure transducers (PPTs) at various locations on the device interface, as illustrated in Fig. 2. Four transducers are installed at the tip of the toroid, referred to here as the invert position (“inv”). The hemiball features five pressure transducers, with two sensors at the intermediate (“int”; $\theta = 22.5^\circ$) and midface (“mf”; $\theta = 45^\circ$) locations and one at the device tip. The pore pressure sensors allow the dissipation characteristics of the soil to be measured and facilitate effective stress interpretations of the rotation stage. For larger penetrometers, intended for direct in situ deployment via a seabed frame or ROV, additional pore pressure sensors could be added at different locations on the device surface. Schneider et al. (2020a) describe in more detail the penetrometers and the actuator developed to operate them.

Fig. 2. Illustration of shallow penetrometers and terminology used for (a) hemiball and (b) toroid (after Schneider et al. 2020a; reprinted with permission from ASTM Geotechnical Testing Journal, Volume 43, copyright ASTM International, 100 Barr Harbor Drive, West Conshohocken, PA 19428, www.astm.org). *int*, intermediate location; *inv*, invert position; *mf*, midface location.



Envisaged testing stages

A single test is sufficient to deduce the key soil parameters required for contemporary pipeline design (Det Norsk Veritas 2007). The tests are relatively brief and thus suitable for in situ box-core testing on a site investigation vessel, during either a geophysical or geotechnical site survey. Table 1 shows the envisaged testing stages alongside the soil properties that can be estimated in each phase. The strength (s_u) and dissipation characteristics (c_v) are evaluated in the penetration and consolidation stages, respectively. The rotation stage and variations of it are used to evaluate the frictional penetrometer–soil interaction properties (τ_u , δ). Friction characteristics of the sediment ($s_{u,int}$, ϕ') can be assessed directly using a device with a completely rough interface (average surface roughness, $R_a > 100 \mu\text{m}$; Meyer et al. 2015). Once all excess pore-water pressures have dissipated after a sufficiently long rotation phase, the device can be subjected to additional penetration to generate a measure of the consolidated undrained shear strength ($s_{u,c}$).

Interpretation of penetration and dissipation stages

Undrained penetration

With regards to pipelines, undrained conditions apply for penetration at dimensionless velocities, V_{pen} , greater or equal to ~ 100 (Chatterjee et al. 2013). The dimensionless velocity is expressed as a function of the penetration speed, v_{pen} , the device diameter, D , and the coefficient of consolidation, c_v , as

$$(1) \quad V_{pen} = \frac{v_{pen} D}{c_v} \geq 100$$

When planning a shallow penetrometer test routine, the following considerations regarding the target penetration depth, w , need to be taken into account:

1. Select w/D so that effective normal stresses on the interface of the device are within the range of practical interest (after dissipation), which is typically $\sim 5\text{--}20 \text{ kPa}$ for subsea pipelines (e.g., push device to $w/D = 0.3$ and unload to project-relevant stress level if excessive resistance is experienced).
2. Target $0.15 \leq w/D \leq 0.5$ so that the geometric similarity between the shallow penetrometer and subsea pipelines is achieved (e.g., initial penetration to $w/D = 0.3$ would provide some allowance for additional settlement during the dissipation and rotation stage, whilst keeping $w/D \leq 0.5$).
3. For the hemiball, ensure $w/D \geq \sim 0.15$ so that the midface pressure transducers are fully embedded in soil at the end of the penetration stage.

For interpretation of the penetration stage, the linear model of Stanier and White (2015), which was developed from an extensive LDFE study of shallow penetrometer penetration in fine-grained sediments for undrained conditions, is used to convert the mea-

Table 1. Targeted soil properties of shallow penetrometer testing stages.

Main testing			
Phase	Description	Relevant measure	Properties of interest
1	Penetration	V , w	s_u , ($s_{u,rem}$)
2	Consolidation	u	c_v
3	Rotation	T , u , w	τ_u , δ , ϕ' , (κ/λ)*
4	(Extra penetration)	V , w	($s_{u,c}$)

Note: Brackets indicate potential measurements not considered in the scope of this paper. V , measured vertical load; w , recorded probe embedment; u , pore-water pressure; T , mobilized torque; $s_{u,rem}$, remoulded shear strength; κ/λ , elastic-plastic volumetric stiffness ratio.

*Different properties can be evaluated based on rotation rate, device actuation, and roughness.

sured vertical load to a linearly varying undrained shear strength profile. The total vertical penetrometer resistance, V , consists of two components: the geotechnical soil resistance, V_{geot} , and the soil buoyancy, V_b , which are defined as

$$(2) \quad V = V_{geot} + V_b = N_{c,nom} A_{nom} s_{u0} + f_b V_s \gamma'$$

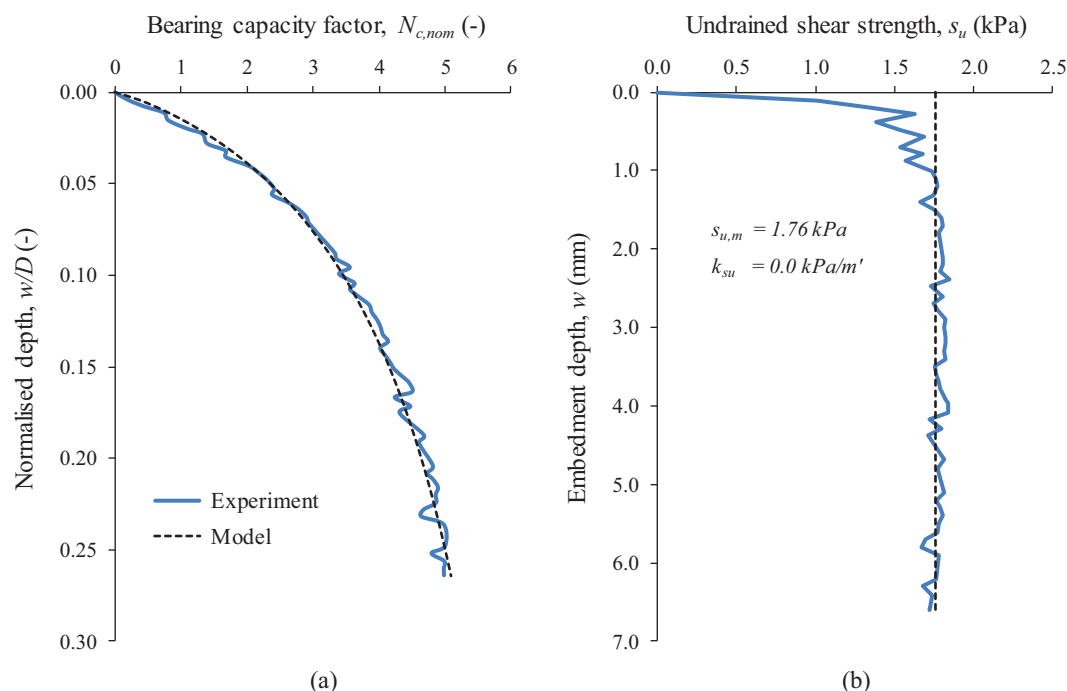
In the geotechnical resistance term, $N_{c,nom}$ is a bearing capacity factor, A_{nom} is the nominal bearing area ($\pi D^2/4$ and $2\pi LD$ for the hemiball and toroid, respectively), and s_{u0} is the undrained shear strength at the current depth of the invert of the device. In the soil buoyancy term, f_b is an enhancement factor that accounts for the relative increase in resistance beyond Archimedes' principle that is caused by local soil heave around the periphery of the device, V_s is the volume of soil displaced by the penetration of the device (embedded volume relative to original mudline), and γ' is the effective unit weight of the soil.

The model is used to evaluate the mudline strength, $s_{u,m}$, as well as the strength gradient, k_{su} , by performing iterations until the measured and theoretical profiles align. The bearing capacity factor, $N_{c,nom}$, is estimated iteratively as a function of the normalized embedment, w/D , and the strength parameter $s_{u,avg}$, which is the average shear strength between the mudline and a depth of one penetrometer diameter (i.e., $s_{u,avg} = s_{u,m} + 0.5k_{su}D$). Figure 3 demonstrates this back-analysis method for a toroid test, eventually leading to an excellent match between test measurements and the analytical model. More information regarding the procedure is found in Stanier and White (2015).

Cyclic penetration: cyclic remoulding test (CRT)

The cyclic remoulding test (CRT) is a variation of the monotonic penetration test where the device is cyclically penetrated into and out of the soil at an undrained penetration rate ($V_{pen} \geq 100$) in an attempt to mimic the effects of pipe-laying processes (10 penetration-extraction cycles with an amplitude of $0.15D$ were modelled in this

Fig. 3. Illustration of back-analysis procedure proposed by Stanier and White (2015) for a toroid test: (a) bearing capacity factor model fit and (b) derived undrained strength profile. [Colour online.]



study). In addition to the initial undrained strength profile of the soil, a measure of the remoulded strength, $s_{u,rem}$, and the soil sensitivity, S_r , may be derived. Examples of this variant of penetration test are presented later in this paper.

Consolidation stage

For the consolidation stage, the vertical load recorded at the final penetration depth is held constant (load-controlled mode: $V = V_{max}$) to mimic the self-weight of a pipe-like structure. The coefficient of consolidation can be estimated reliably if the dissipation process is monitored until at least 50% of the initial excess pore pressures have dissipated (i.e., final drainage index $\psi > 0.5$, with $\psi = 1 - (\Delta u / \Delta u_{ini})$). This provides a sufficient proportion of the dissipation response to allow accurate fitting to the theoretical solution, using the same approach as is common for cone penetrometer dissipation tests. However, if the undrained interface strength of the seabed is to be determined after full consolidation under the weight of a pipe or foundation in the subsequent rotation stage, it is better to allow >90% of the initial excess pore pressures to dissipate (i.e., where the final drainage index $\psi > 0.9$). The general dissipation response of soil can be fitted with a hyperbolic function in terms of the normalized excess pore pressure as follows:

$$(3) \quad \frac{\Delta u}{\Delta u_{ini}} = \frac{1}{1 + (T_{dis}/T_{dis,50})^m} \quad \text{where } T_{dis} = \frac{c_v t_{dis}}{D^2}$$

The dimensionless time, T_{dis} , is a function of the consolidation coefficient, c_v ; the dimensional dissipation time, t_{dis} ; and the penetrometer diameter, D . The shape of the hyperbolic relationship is governed by the parameters m and $T_{dis,50}$ (dimensionless time at which ~50% of consolidation has finished), which are fitting parameters derived from numerical simulations. Rearrangement of eq. (3) leads to the following expression:

$$(4) \quad t_{dis} = \frac{D^2 T_{dis,50}}{c_v} \left(\frac{\psi}{1 - \psi} \right)^{1/m}$$

which can be used to estimate the timescales of shallow penetrometer dissipation tests for particular values of the coefficient of consolidation, c_v .

The fitting parameters in eqs. (3) and (4) can be defined in terms of the dissipation response at a specific transducer location on the device interface ($T_{dis,50}$ and m) or the average pore pressure dissipation on the embedded penetrometer surface ($T_{dis,50,ave}$ and m_{ave}). The parameters associated with a specific spot measurement (here: invert location) are of practical relevance for determining the coefficient of consolidation of soil, whereas the parameters characterizing the periphery dissipation response can be used to estimate timescales (e.g., for the increase in friction around the device due to the drainage of excess pore pressures).

Yan et al. (2017) published SSFE solutions for both the “invert” and “average” values, which can be used in conjunction with eqs. (3) or (4). The hemiball and toroid solutions given are based on wished-in-place simulations (in other words, the soil that would have occupied the final position of the penetrometer (including shaft) is simply replaced by the penetrometer) developed using the Modified Cam Clay (MCC) soil model, hence ignoring the influence of penetration-induced soil heave around the penetrometer.

LDFE-modelling techniques provide more realistic results, as the propensity for soil heave and other influences of the penetration process are captured. Yan et al. (2011a) showed that a toroid with an aspect ratio, L/D , of 2 or higher experiences from minimal to no interference across the device, meaning that pipeline solutions can be adopted with sufficient accuracy (e.g., LDFE pipeline solutions after Chatterjee et al. 2012, as specified in Table 2). No LDFE dissipation solutions for a rough hemiball have been published to date. To address this gap, LDFE simulations modelling the process of excess pore pressure dissipation around a rough hemiball were conducted, as presented in the next section.

An example application of eq. (3) using the coefficients in Table 2 is given in Fig. 4 for a toroid test performed on kaolin clay. Figure 4a shows raw dissipation measurements for all four PPTs, which are at equidistant circumferential locations around the toroid at the penetrometer invert. The measured average excess

Table 2. Hyperbolic fits of dissipation response at penetrometer invert (normally consolidated soils).

w/D	LDPE solutions			
	Toroid (rough)*		Hemiball (rough)	
	$T_{dis,50}$	m	$T_{dis,50}$	m
0.1	0.028	1.05	This study (see also Table 4)	
0.2	0.055	1.05		
0.3	0.075	1.05		
0.4	0.110	1.05		
0.5	0.135	1.05		

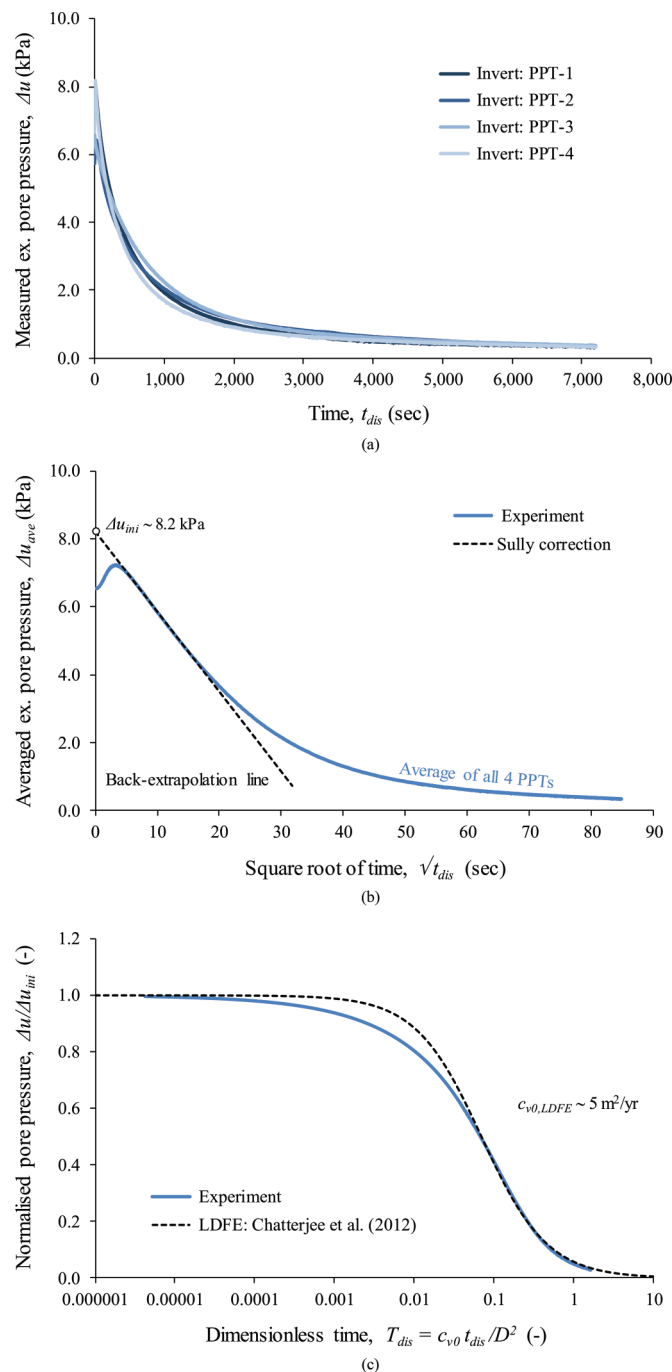
*Values after Chatterjee et al. (2012), assuming that a toroid is equivalent to a pipe for $L/D \geq 2$.

pore pressure is then corrected for measurement lag according to the procedure proposed by Sully et al. (1999), as illustrated in Fig. 4b. The initial excess pore pressure value, Δu_{ini} , is derived via back-extrapolation of the (averaged) test measurements in root-time space. The coefficient of consolidation corresponding to the depth of the penetrometer invert, c_{v0} , can then be estimated by fitting the normalized dissipation response to a theoretically derived finite element (FE) solution (e.g., Table 2) at $\Delta u/\Delta u_{ini} \sim 0.5$ for the current embedment (with model coefficients interpolated from the listed values, if necessary), as illustrated in Fig. 4c.

New dissipation solutions for hemiball (LDPE)

The following solutions were generated using the “remeshing and interpolation technique with small strains” (RITSS) methodology after Hu and Randolph (1998), which was implemented in the FE software package ABAQUS (Dassault Systèmes 2011), using a combination of Python and FORTRAN scripts, similar to the approach described in Wang et al. (2010). The large-deformation modelling procedure simulates the undrained penetration stage as a series of consecutive small increments to avoid significant mesh distortions. After every calculation step the model domain is remeshed and all stress and state parameters are transferred to the new mesh for the next step, adopting the super-convergent patch recovery method after Zienkiewicz and Zhu (1992) and FE shape functions based interpolation techniques. The same procedure was used to define the initial conditions of the dissipation phase (geometry, stress, and state parameters at the end of the LDPE penetration stage transferred to a new mesh), which was then modelled as a single small-strain simulation.

The shallow penetrometer and soil were modelled using axial symmetry with free distances to the domain boundaries that were sufficiently large to minimize boundary effects (radius: $\sim 8D$; depth: $\sim 10D$). To capture the penetration-induced pore pressure generation and dissipation in normally consolidated soil representative of deep water sediments, the MCC soil model of Roscoe and Burland (1968) was used in conjunction with the soil parameters listed in Table 3. The earth pressure coefficient, K_0 , was estimated empirically as $1 - \sin \phi'_{cv}$ ($K_0 \sim 0.6$). Selection of reduced-integration, quadrilateral coupled pore pressure elements (type: CAX8RP) and enforcement of a minimum applicable time increment (Vermeer and Verruijt 1981; Dassault Systèmes, 2011) led to significantly shorter calculation times and improved solution stability compared to triangular elements. A mesh refinement algorithm was developed to control the maximum element size generated along the device interface during the periodic remeshing process. The mudline was specified as fully draining via a user subroutine, by prescribing hydrostatic conditions (relative to the original intact mudline) to any surface boundary node that was not in direct contact with the penetrometer. Drainage was precluded where the penetrometer was in contact with the soil. The “rough” contact formulation was used to model the coarse surface

Fig. 4. Example back-analysis for dissipation stage: (a) raw pore pressure measurements, (b) back-extrapolation (after Sully et al. 1999), and (c) estimation of coefficient of consolidation. [Colour online.]

texture of the current hemiball device. A small surcharge, q_0 , of ~ 1 kPa (quasi-uniform conditions of s_u and c_v over depth range of interest, as $q_0/\gamma'D = 2$) was required to achieve convergence at the free surface of the soil and to create a shear strength intercept at the mudline. The appropriateness of the adopted mesh density and penetration rate ($V_{pen} \sim 100$) was confirmed through sensitivity analyses (see also Schneider et al. 2019).

Undrained penetration resistance

Rearrangement of eq. (2) allows the normalized penetration resistance, $N_{c,nom}$, to be expressed as

Table 3. Modified Cam Clay parameters assumed (Stewart 1992).

Assumed soil parameter	Value
Critical state constant, M	0.92
Void ratio on CSL (at $p' = 1$ kPa), e_{cs}	2.14
Slope of normal consolidation line, λ	0.205
Slope of swelling line, κ	0.044
Poisson's ratio, ν	0.30
Soil permeability, k (m/s)	1×10^{-9}
Effective unit weight, γ' (kN/m ³)	5.0
Overconsolidation ratio, OCR	1.0
Unit weight of water, γ_w (kN/m ³)	10

Note: CSL, critical state line.

$$(5) \quad N_{c,nom} = \left(\frac{V_{geot}}{A_{nom}s_{u0}} \right) = \left(\frac{V}{A_{nom}s_{u0}} \right) - f_b \left(\frac{\gamma' V_s}{A_{nom}s_{u0}} \right)$$

where $A_{nom} = \frac{\pi D^2}{4}$

Figure 5 shows the numerically derived resistance for the initial undrained penetration phase, up to an embedment of $0.5D$. Solutions published by Stanier and White (2015) were used to determine the buoyancy factor, f_b , as a function of embedment, and hence submerged penetrometer volume, V_s . The undrained shear strength, s_{u0} , at the normalized embedment of the penetrometer invert, w/D , was estimated according to Wood (1990) as a function of the MCC parameters indicated in Table 3.

Chatterjee et al. (2014) reported results for the penetration of the “parkable piezoprobe”, which are comparable to the smooth hemiball calculations as the geometry of the two devices is the same, thus validating the FE model used (Fig. 5). Large-deformation Tresca analyses were published by Stanier and White (2015), for both a smooth and rough hemiball. The lower penetration resistance (roughly ~15%–20%) exhibited in the Tresca simulations of Stanier and White (2015) may be attributed to (i) the difference in yield surface shape between the two models (Tresca hexagon vs. circumscribing von Mises circle in the deviatoric plane giving a maximum deviation of ~15% under plane strain conditions) and (ii) an underprediction of the failure load due to the Tresca–Mises hybrid criterion implemented in the Mohr–Coulomb/Tresca model in ABAQUS (Taiebat and Carter 2008).

Minor drainage and local re-distribution of excess pore pressures is also unavoidable during the penetration stage (MCC simulations) and may further increase the differences between the two genera of simulations.

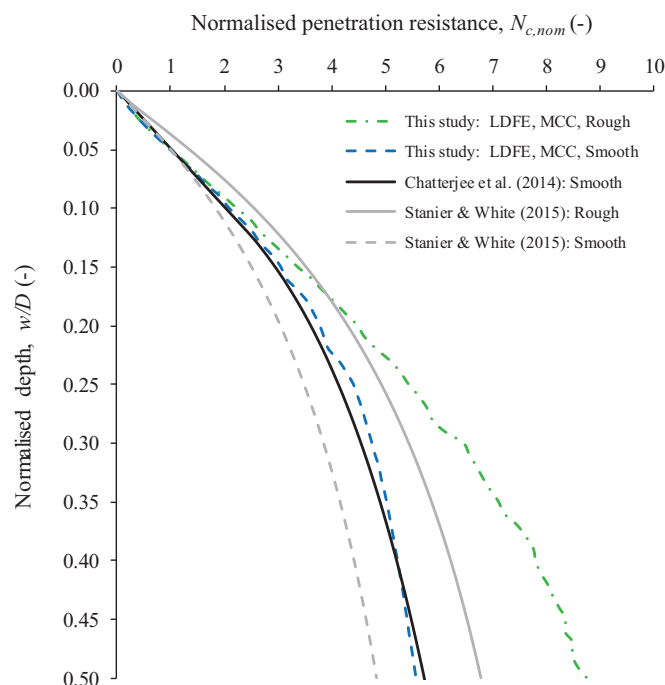
Dissipation solutions

The nondimensional dissipation response is shown in Fig. 6 for a normalized embedment, w/D , of 0.3 and at three transducer locations. Just as for the results in Table 2, the solutions were normalized using the value of c_{v0} (coefficient of consolidation at penetrometer invert) defined as

$$(6) \quad c_{v0} = \frac{k}{m_v \gamma_w} = \frac{k(1 + e_0)p'_0}{\lambda \gamma_w}$$

The compressibility index, m_v , can be expressed as a function of the stiffness parameter, λ (the slope of normal consolidation line); the initial mean effective stress, p'_0 ; and the initial void ratio, e_0 .

New dissipation solutions were created via curve-fitting of the numerical LDFF data, using the hyperbolic relationship given in eq. (3). Table 4 lists the $T_{dis,50}$ and m values determined for the invert, intermediate, and midface positions at various normalized embedment depths. No values are specified in instances where

Fig. 5. Comparison of undrained penetration resistance for different LDFF solutions: MCC (this study and Chatterjee et al. 2014) vs. TRESCA solutions (Stanier and White 2015). [Colour online.]

the sensor location was too close to the mudline, which leads to an inconsistent dissipation response.

The dissipation responses for all three transducer locations defined in Table 4 are normalized by the same coefficient of consolidation, c_{v0} , representative of intact soil conditions at the penetrometer invert for each normalized embedment depth, w/D . Consequently, back-analyses of a hemiball test should yield similar c_{v0} values for the three pore pressure sensor locations if the model is robust, as will be demonstrated later in the paper.

Figure 6 shows that a significant Mandel–Cryer effect (Mandel 1950; Cryer 1963), which is revealed by the initial rise in excess pore pressure, is only observed at the invert position of the penetrometer and not at the other two transducer locations (Mandel–Cryer effect, with the observed rise in excess pore pressure due to a local increase in total stress during the early stages of the dissipation process). This phenomenon occurred for all embedment ratios, w/D , as also found in other studies of shallow penetration of rough structures (e.g., Chatterjee et al. 2012). For the invert solution, the hyperbolic model of eq. (3) was fitted to the simulation data for $\Delta u/\Delta u_{ini} \leq 0.9$, essentially ignoring the Mandel–Cryer effect.

Experimental testing programme

Sample preparation and characterization

Four soft kaolin clay samples were consolidated in large strong-boxes (length: 1300 mm; width: 390 mm) under an effective stress of ~20 kPa, before unloading and swelling to equilibrium. This stress history yields samples with undrained strength of 1–2 kPa, approximately constant over the depth range of the tests, which is broadly representative of the strength of soft surficial clay found offshore in deep water locations (e.g., Randolph et al. 2018).

T-bar tests ($D_{Tbar} = 5$ mm) were conducted in each of the samples prior to shallow penetrometer testing. Each test ensured undrained penetration, with a penetration rate of $V_{pen} = v_{pen} D_{Tbar}/c_v > 30$ after Finnie and Randolph (1994), and included 10 penetration–extraction cycles to assess the soil sensitivity. All soil samples were found to be laterally homogeneous, as the recorded soil strength profiles were

Fig. 6. Normalized dissipation response for hemiball penetrometer ($w/D = 0.3$). [Colour online.]

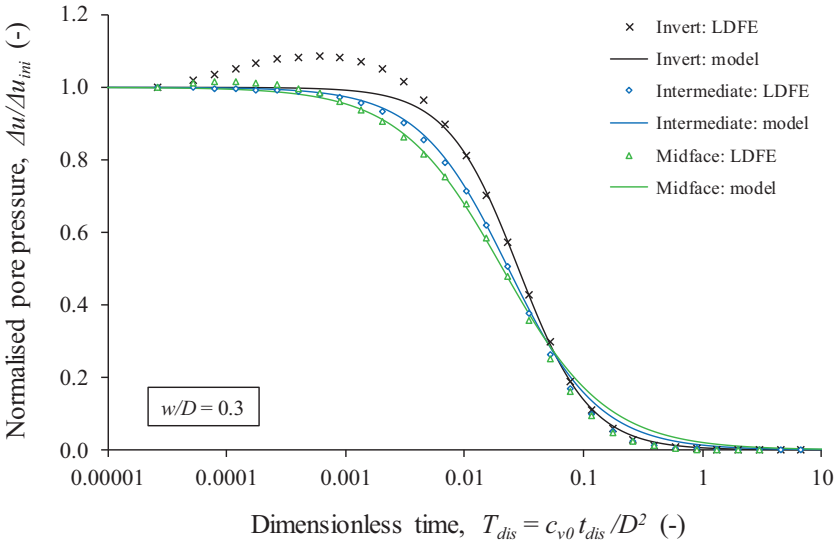


Table 4. Hyperbolic fits corresponding to new rough hemiball LDFE dissipation solutions at different penetrometer locations.

w/D	Invert sensor		Intermediate sensor		Midface sensor	
	$T_{dis,50}$	m	$T_{dis,50}$	m	$T_{dis,50}$	m
0.10	0.0105	1.50	—	—	—	—
0.20	0.0200	1.45	0.0160	1.20	—	—
0.30	0.0285	1.45	0.0235	1.15	0.0210	1.00
0.40	0.0320	1.35	0.0275	1.10	0.0295	1.20
0.50	0.0335	1.30	0.0305	1.10	0.0315	1.20

practically uniform within each strongbox. Likewise, the measurements were also consistent across all four strongboxes, thus allowing direct comparison of the results of different shallow penetrometer tests, independent of the exact testing location or the strongbox in which they were performed. Small soil specimens, recovered with the miniature core sampler, were also analysed at the end of each testing session to provide the moisture content and thus void ratio and effective unit weight of the samples.

Shallow penetrometer testing

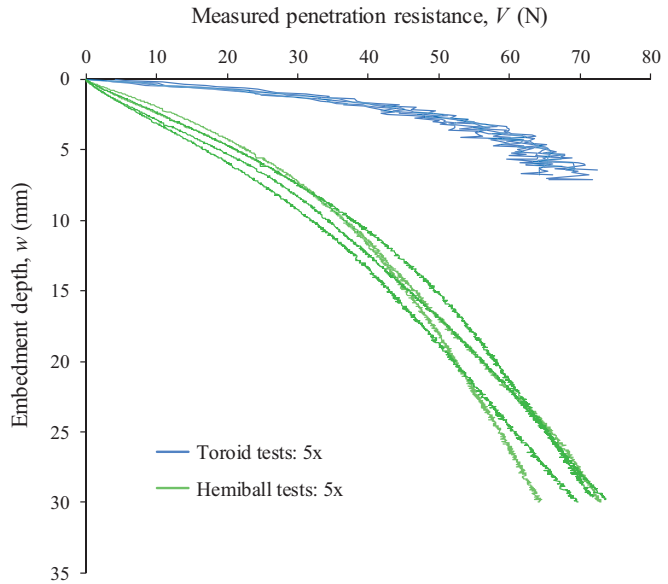
Due to the larger diameter of the hemiball ($D = 100$ mm), only four penetrometer tests could be performed in each strongbox whilst ensuring minimal boundary or interaction effects. For the toroid ($D = 25$ mm), five tests were possible. The greater number of toroid tests was possible because the absolute embedment depths (and hence soil disturbance) were much lower even though the normalized embedment may be the same for both penetrometers (e.g., $w/D = 0.3$). The volume of soil displaced by the hemiball is significantly larger than for the toroid, which results in spatially more expansive failure mechanisms.

Undrained penetration

An initial embedment at the end of the penetration stage of $w/D = 0.3$ was targeted. This provided some allowance for settlement during dissipation and rotation, whilst keeping $w/D \leq 0.5$. For the samples tested it also resulted in effective normal contact stresses on the shallow penetrometers in the range of 5–15 kPa, which spans the operating range for typical subsea pipelines.

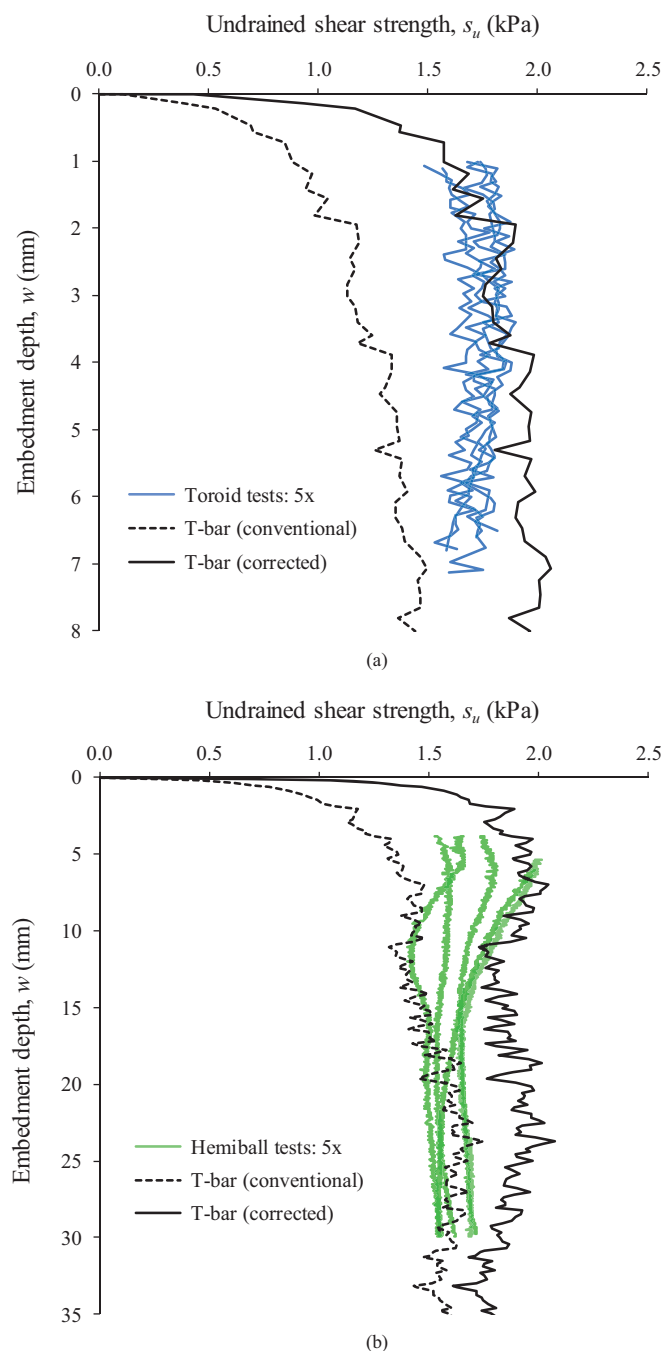
Figure 7 shows the measured undrained penetration resistance for five hemiball and five toroid tests (for clarity, only five tests are presented here for each device, although the unreported data sets yielded very similar results), with both devices approaching a sim-

Fig. 7. Measured penetration resistance for five hemiball and toroid tests. [Colour online.]



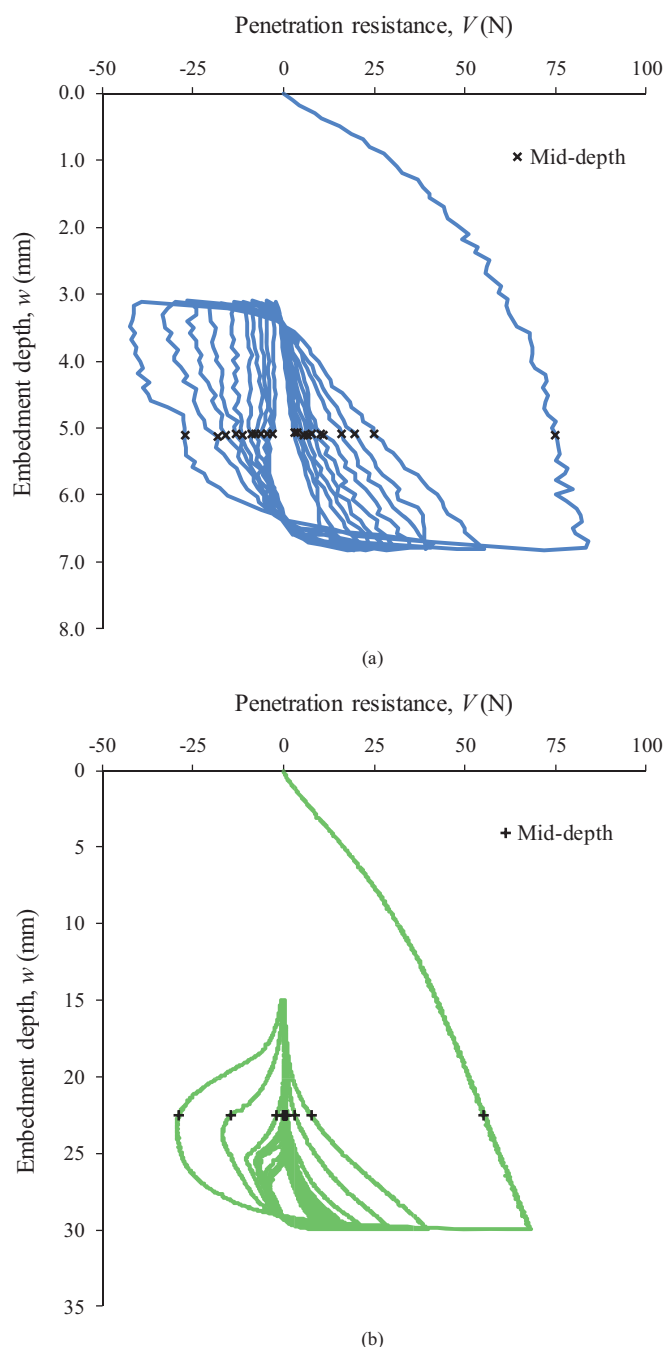
ilar failure load at the target embedment of $w/D = 0.3$. All shallow penetrometer tests yield comparable strength profiles, thus demonstrating high repeatability and resolution. The penetration rate required to ensure undrained conditions is significantly faster for the toroid due to its smaller diameter, thus leading to slightly more measurement noise, as can be seen in Figs. 7 and 8.

Fig. 8. Results of undrained penetration phase: undrained shear strength vs. embedment for (a) toroid and (b) hemiball penetrometers. [Colour online.]



The procedure of Stanier and White (2015) was used to convert the measured vertical load, V , into the corresponding strength profiles. The inferred soil strength profiles, for both the toroid and hemiball penetrometer, are in excellent agreement with each other (Fig. 8). Independent T-bar test measurements, with and without shallow corrections after White et al. (2010a), are plotted alongside the penetrometer tests to provide context. The shallow penetrometer measurements are bracketed by the strength profiles determined via the conventional uncorrected method, assuming a bearing factor, $N_t = 10.5$ (Stewart and Randolph 1991), and the shallow corrected T-bar interpretation method.

Fig. 9. Undrained cyclic penetration resistance: (a) toroid and (b) hemiball penetrometers. [Colour online.]

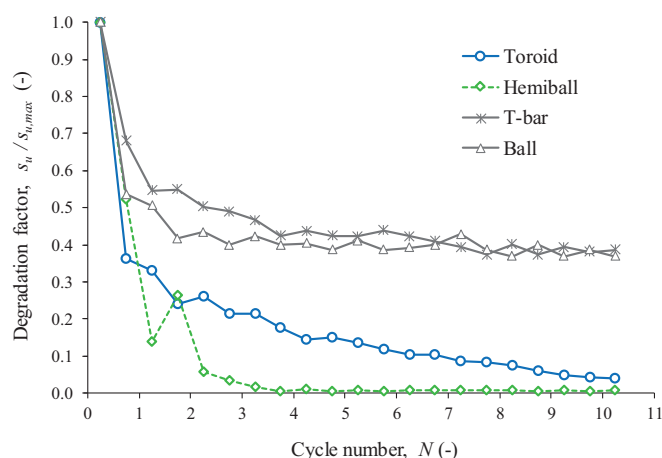


Cyclic penetration

The purpose of the CRTs is to emulate seabed disturbance such as the pipe-laying process. Ten penetration–extraction cycles of $0.15D$ amplitude were conducted after the initial penetration to $0.3D$, i.e., with embedment depths ranging between $\sim 0.15D$ and $\sim 0.3D$. Figure 9 shows that the penetration and extraction responses differ significantly for the two shallow penetrometer geometries tested. A major degradation of undrained strength and correspondingly large “apparent” sensitivities, $S_t = s_u/s_{u,rem} \gg 10$, were observed for both penetrometers (Fig. 10). This is much higher than found in comparative (deeply embedded) T-bar and ball cyclic penetrometer tests, for which $S_t \sim 2.5$.

It is clear from Fig. 9 that the interpretation of strength degradation depends strongly on the adopted interpretation depth. All

Fig. 10. Degradation of undrained soil strength for toroid, hemiball, T-bar, and ball penetrometers. [Colour online.]



data points presented in Fig. 10 were taken at the mid-depth of each cycle, as indicated in Fig. 9 by the black markers. The bearing capacity factor, $N_{c,nom}$, required to estimate the undrained shear strength was assumed equal to that found for the initial monotonic penetration, at the same embedment depth and for all cycles. Results of a cyclic T-bar (diameter: 5 mm, length: 20 mm, $N_t = 10.5$) and a ball penetrometer test (diameter: 10 mm, $N_b = 10.5$ after Chung and Randolph 2004) are plotted alongside the shallow penetrometer measurements for comparison purposes (Fig. 10).

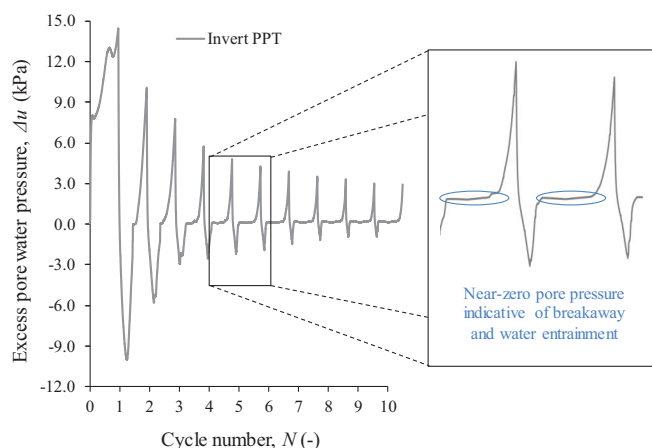
Close scrutiny of the excess pore pressure measurements revealed that water entrainment was most likely responsible for the massive strength degradation, as well as the formation of an indentation in the seabed. Near-zero pore pressure readings — indicative of break-away on extraction and subsequently water entrainment on re-penetration — are seen in Fig. 11 for the invert transducer of the hemiball after only a few cycles of penetration.

It remains an open question as to which of the cyclic remoulding tests is most applicable for predicting the pipe-laying process: deep penetrometer tests such as the T-bar and ball penetrometer or the shallow penetrometer tests. Previous case studies of an offshore pipeline indicated that the “as-laid” embedment was best predicted using the remoulded strength measured using a miniature T-bar, and this has been confirmed by a wider dataset (Westgate et al. 2012; White et al. 2017). The small-amplitude movements of a shallow penetrometer test are more representative of the pipe-laying process, where water entrainment is highly probable (Sahdi et al. 2014), but the formation of a seabed indentation beneath the penetrometer hampers interpretation of data such as shown in Fig. 9. Given the experience using conventional T-bar penetrometer tests for as-laid embedment predictions, the role of cyclic shallow penetrometer tests is to provide additional information such as the dissipation characteristics following remoulding and water entrainment as well as the sliding friction determined during the rotation phase.

Pore pressure dissipation

The penetration stage is followed by a load-controlled (LC) consolidation phase. The aim in this study was to allow almost complete dissipation of the penetration-induced excess pore pressures, with the vertical load applied to the penetrometer kept constant throughout at the load recorded at the final penetration depth, $V_{max} = f(w/D = 0.3)$, thereby simulating the self-weight of a pipe-like structure on the ocean floor. The durations of the consolidation phases were 2 and 4 h for the toroid and hemiball penetrometer, respectively. A total of eight toroid and eight hemiball tests were carried out, although only the results of the latter six hemiball tests are presented here. This is because for the first two hemiball

Fig. 11. Breakaway and water entrainment for invert PPT of hemiball penetrometer. [Colour online.]

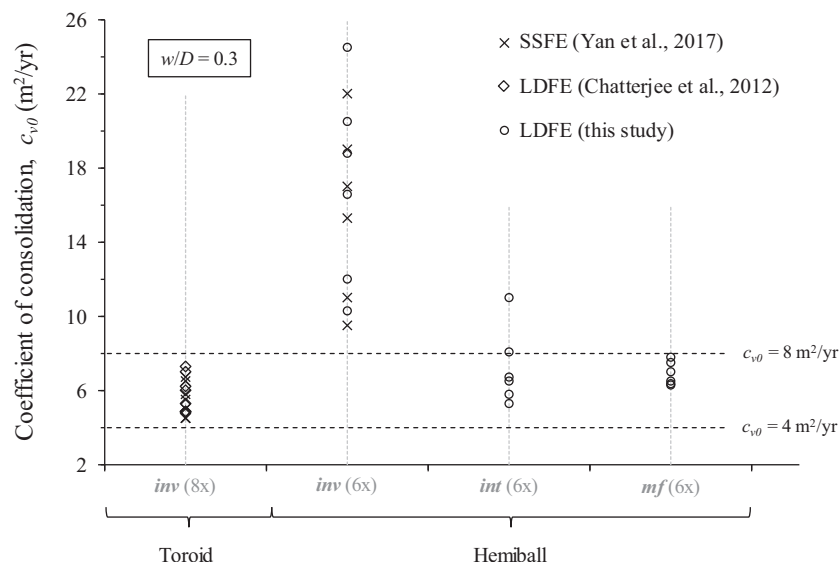
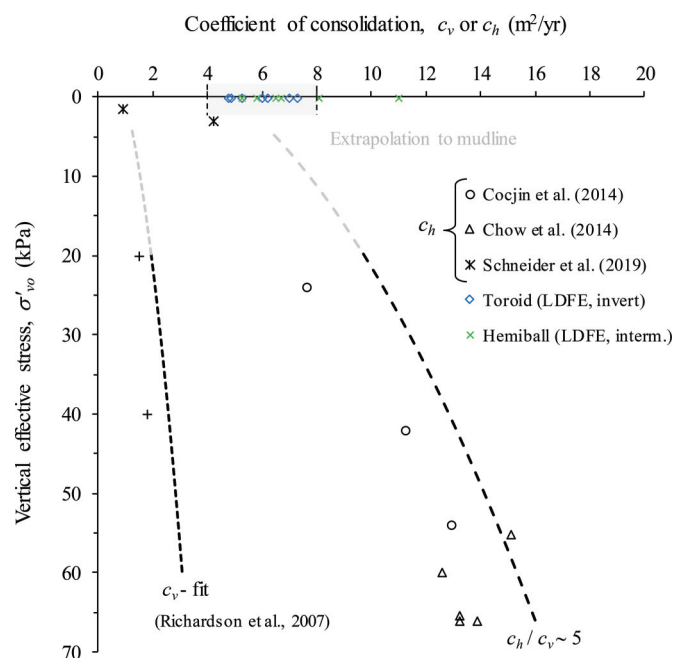


tests, silicone oil was used to backfill the pressure transducers, which resulted in clogging of the porous plastic filters used to shield the sensing elements, eventually leading to a drift in the pore pressure measurements. Investigation into different back-filling liquids revealed that de-aired water was least affected by clogging in fine-grained sediments (Schneider et al. 2020a).

The excess pore pressure measurements were interpreted using the methodology described earlier and the model coefficients given in Tables 2 and 4, with both penetrometers yielding very similar coefficients of consolidation, c_{v0} . This is in spite of the fact that the dimensional dissipation response for the toroid is significantly faster than for the hemiball, due to the four-fold difference in device cross-sectional dimensions. This is evidence of the robustness of the interpretation model proposed. Figure 12 shows a summary of the values inferred from the different dissipation solutions stated in Tables 2 and 4 (including c_{v0} values obtained from dissipation measurements following both a monotonic and a cyclic penetration stage).

Excellent test repeatability is evident for the dissipation response. Most inferred coefficients of consolidation lie within a relatively close range of $c_{v0} = 4\text{--}8 \text{ m}^2/\text{year}$, irrespective of the device used, with only the values corresponding to the invert response of the hemiball deviating from this range. The SSFE wished-in-place dissipation solutions published by Yan et al. (2017) yield almost identical values to the LDFE solutions presented by Chatterjee et al. (2012) and the hemiball solutions provided in this paper, in spite of the LDFE simulations better capturing peripheral soil heave. This confirms that soil heave around the periphery of the penetrometers has minimal influence on the dissipation characteristics. The fact that very similar c_{v0} values were found for both test variations (monotonic or cyclic penetration prior to dissipation), suggests that the remoulding cycles seemed to affect the soil only very locally (close to the probe interface). The coefficient of consolidation inferred therefore seems to be governed mainly by the intact soil state rather than by the remoulded condition.

A good match between the shapes of the numerically (SSFE and LDFE) and experimentally derived dissipation responses was found for both penetrometers and all transducer locations (e.g., Figure 4c), except for the invert position of the hemiball, where a noticeable difference in shape was encountered. Moreover, there is no measurement redundancy for this position as there can only be a single pressure sensor in that location. Consequently, it is recommended that the LDFE dissipation solutions corresponding to the invert and intermediate locations for the toroid and hemiball, respectively, be used, taking advantage of averaging through the use of multiple transducers. The readings recorded by the midface hemiball transducers are often negatively affected by the

Fig. 12. Overview of inferred coefficients of consolidation for toroid and hemiball.**Fig. 13.** Coefficient of consolidation in kaolin clay: inferred values vs. existing literature. [Colour online.]

proximity to the mudline. However, if the penetrometer is sufficiently embedded, the midface measurements can also provide independent estimates of the coefficient of consolidation.

Figure 13 compares the inferred coefficients of consolidation with miniature piezocone (c_h) and Rowe cell (c_v) data measured independently in the same kaolin clay over the past decade or more at The University of Western Australia (Richardson 2007; Chow et al. 2014; Cocjin et al. 2014). Data at shallow embedment are conspicuously absent, but the shallow penetrometer data presented here are consistent with the measurements generated using the parkable piezoprobe, another device intended to measure surficial soil properties (Chatterjee et al. 2014; Schneider et al. 2019) and the back-extrapolated trends from the piezocone and Rowe cell data.

Conclusions

This paper has shown that the strength and consolidation properties of soft surficial soil can be estimated reliably with shallow penetrometers, such as the box-core sized toroid and hemiball. The fundamentals of the penetration and dissipation stages, alongside the geotechnical relationships needed to back-analyse such tests, were highlighted. Furthermore, new large-deformation finite element (LDFE) dissipation solutions exploring the impact of local peripheral heave on the dissipation response for the hemiball and a comprehensive laboratory testing programme in kaolin clay were presented. The key findings can be summarized as

- Results of the laboratory testing session demonstrate that both penetrometers are capable of providing accurate estimates of undrained strength and consolidation characteristics of fine-grained surficial sediments. Excellent test repeatability was demonstrated and the interpretation models were shown to be robust, with all results in excellent agreement with each other and consistent with the existing literature.
- Simple interpretations of the undrained soil strength profiles can be obtained for design purposes using the model of Stanier and White (2015). The methodology yields very comparable results to miniature T-bar measurements.
- Back-analysis of the experiments demonstrates that the LDFE hemiball dissipation solutions presented here yield consistent estimates for the coefficient of consolidation. Additional outcomes include (i) the preferred use of the pore pressure measurements recorded at the intermediate hemiball transducer location and (ii) the observation that soil heave around the periphery of the penetrometers has minimal influence on the dissipation response.
- Deeper insight into the effect of the pipe-laying process can be gained by executing undrained penetration – extraction cycles. The extreme strength degradation observed in these tests warrants further exploration of the potential impact of water entrainment during pipe-laying in estimating pipeline embedment. An experimental study investigating the influence of the cycling rate and amplitudes on the strength, deformation, and dissipation characteristics of fine-grained soils would be a logical next step. Consequently, it is suggested that a conventional miniature full-flow penetrometer continue to be used to assess soil sensitivity, rather than a cyclic shallow penetrometer test.

Acknowledgements

The research presented here forms part of the activities of the Centre for Offshore Foundation Systems (COFS), currently supported as a node of the Australian Research Council (ARC) Centre of Excellence for Geotechnical Science and Engineering (CE110001009). The first author is grateful for the support provided by an International Postgraduate Research Scholarship (IPRS) from the Australian Government. The second author was supported by an ARC DECRA Fellowship (DE170100119). This work has been further supported by Shell, via the Shell EMI Chair in Offshore Engineering held by the third author, and by Fugro via the Fugro Chair in Geotechnics held by the fourth author. The authors are also grateful for the support from the RIGSS JIP partners: Fugro, Shell, Total, and Woodside Energy.

References

- Baligh, M.M., Azzouz, A.S., and Chin, C.-T. 1987. Disturbances due to "ideal" tube sampling. *Journal of Geotechnical Engineering*, **113**(7): 739–757. doi:10.1061/(ASCE)0733-9410(1987)113:7(739).
- Chatterjee, S., Yan, Y., Randolph, M.F., and White, D.J. 2012. Elastoplastic consolidation beneath shallowly embedded offshore pipelines. *Géotechnique Letters*, **2**: 73–79. doi:10.1680/geolett.12.00031.
- Chatterjee, S., White, D.J., and Randolph, M.F. 2013. Coupled consolidation analysis of pipe-soil interactions. *Canadian Geotechnical Journal*, **50**(6): 609–619. doi:10.1139/cgj-2012-0307.
- Chatterjee, S., Randolph, M.F., and White, D.J. 2014. A parkable piezoprobe for measuring c_v at shallow depths for offshore design. *Géotechnique*, **64**(1): 83–88. doi:10.1680/geot.13.T.008.
- Chow, S.H., O'Loughlin, C.D., and Randolph, M.F. 2014. Soil strength estimation and pore pressure dissipation for free-fall piezocone in soft clay. *Géotechnique*, **64**(10): 817–827. doi:10.1680/geot.14.P.107.
- Chung, S.F. and Randolph, M.F. 2004. Penetration resistance in soft clay for different shaped penetrometers. In *Proceedings of the 2nd International Conference on Site Characterization*, Porto. Vol. 1. pp. 671–677.
- Clayton, C.R.I., Siddique, A., and Hopper, R.J. 1998. Effects of sampler design on tube sampling disturbance-numerical and analytical investigations. *Géotechnique*, **48**(6): 847–867. doi:10.1680/geot.1998.48.6.847.
- Cocjin, M.L., Gourvenec, S.M., White, D.J., and Randolph, M.F. 2014. Tolerably mobile subsea foundations – observations of performance. *Géotechnique*, **64**(11): 895–909. doi:10.1680/geot.14.P.098.
- Cryer, C.W. 1963. A comparison of the three-dimensional consolidation theories of Biot and Terzaghi. *The Quarterly Journal of Mechanics and Applied Mathematics*, **16**(4): 401–412. doi:10.1093/qjmam/16.4.401.
- Dassault Systèmes. 2011. Abaqus analysis user's manual. Simulia Corporation. Providence, RI, USA.
- Det Norske Veritas. 2007. DNV-RP-F110 — Global buckling of submarine pipelines. Det Norske Veritas.
- Finnie, I.M.S., and Randolph, M.F. 1994. Punch-through and liquefaction induced failure of shallow foundations on calcareous sediments. In *Proceedings of the International Conference on Behavior of Offshore Structures*, (BOSS), Boston, Mass. pp. 217–230.
- Hover, E.D., Ni, Q., and Guymier, I. 2013. Investigation of centreline strain path during tube penetration using transparent soil and particle image velocimetry. *Géotechnique Letters*, **3**(2): 37–41. doi:10.1680/geolett.13.00017.
- Hu, Y., and Randolph, M.F. 1998. A practical numerical approach for large deformation problems in soil. *International Journal for Numerical and Analytical Methods in Geomechanics*, **22**(5): 327–350. doi:10.1002/(SICI)1096-9853(199805)22:5<327::AID-NAG920>3.0.CO;2-X.
- Kuo, M.Y.-H., Vincent, C.M., Bolton, M.D., Hill, A., and Rattley, M. 2015. A new torsional shear device for pipeline interface shear testing. In *Frontiers in Offshore Geotechnics III*. Edited by V. Meyer. pp. 405–410.
- Lehane, B.M., and Liu, Q.B. 2013. Measurement of shearing characteristics of granular materials at low stress levels in a shear box. *Geotechnical and Geological Engineering*, **31**: 329–336. doi:10.1007/s10706-012-9571-9.
- Mandel, J. 1950. Étude mathématique de la consolidation des sols. In *Actes du Colloque International de Mécanique*, Poitiers, France. Vol. 4, pp. 9–19.
- Meyer, V., Dyvik, R., and White, D.J. 2015. Direct shear interface tests for pipe-soil interaction assessment. In *Frontiers in Offshore Geotechnics III*. Edited by Meyer. pp. 423–428.
- Morton, J.P., O'Loughlin, C.D., and White, D.J. 2014. Strength assessment during shallow penetration of a sphere in clay. *Géotechnique Letters*, **4**: 262–266. doi:10.1680/geolett.14.00049.
- Pedersen, R., Olson, R., and Rauch, A. 2003. Shear and interface strength of clay at very low effective stress. *Geotechnical Testing Journal*, **26**(1): 71–78. doi:10.1520/GTJ11104J.
- Pineda, J.A., Liu, X.F., and Sloan, S.W. 2016. Effects of tube sampling in soft clay: a microstructural insight. *Géotechnique*, **66**(12): 969–983. doi:10.1680/jgeot.15.P.217.
- Randolph, M.F., Stanier, S.A., O'Loughlin, C.D., Chow, S.H., Bienen, B., Doherty, J.P., et al. 2018. Penetrometer equipment and testing techniques for offshore design of foundations, anchors and pipelines. In *Proceedings of CPT'18 – International Symposium on Cone Penetration Testing*, Delft.
- Richardson, M. 2007. Rowe cell test on kaolin clay, COFS internal report. Centre for Offshore Foundation Systems, The University of Western Australia, Crawley, WA, Australia.
- Roscoe, K.H., and Burland, J.B. 1968. On the generalized stress-strain behaviour of wet clay. In *Engineering Plasticity*, Cambridge. pp. 535–609.
- Sahdi, F., Gaudin, C., and White, D.J. 2014. Strength properties of ultra-soft kaolin. *Canadian Geotechnical Journal*, **51**: 420–431. doi:10.1139/cgj-2013-0236.
- Schneider, M.A., Stanier, S.A., Chatterjee, S., White, D.J., and Randolph, M.F. 2019. The parkable piezoprobe for determining c_v and strength – modelling and interpretation methods. *Géotechnique*, **69**(5): 458–469. doi:10.1680/jgeot.18.P.004.
- Schneider, M.A., Stanier, S.A., White, D.J., and Randolph, M.F. 2020a. Apparatus for measuring pipe-soil interaction behaviour using shallow 'pipe-like' penetrometers. *Geotechnical Testing Journal*, **43**. (Published online ahead of print January 2020.) doi:10.1520/GTJ20180293.
- Schneider, M.A., Stanier, S.A., White, D.J., and Randolph, M.F. 2020b. Shallow penetrometer tests: theoretical and experimental modelling of the rotation stage. *Canadian Geotechnical Journal*, **57**. (In this issue.) doi:10.1139/cgj-2018-0657.
- Stanier, S.A., and White, D.J. 2015. Shallow penetrometer penetration resistance. *Journal of Geotechnical and Geoenvironmental Engineering*, **141**(3): 04014117. doi:10.1061/(ASCE)GT.1943-5606.0001257.
- Stewart, D.P. 1992. Lateral loading of piled bridge abutments due to embankment construction. Ph.D. thesis, The University of Western Australia.
- Stewart, D.P., and Randolph, M.F. 1991. A new site investigation tool for the centrifuge. In *Proceedings of the International Conference on Centrifuge Modelling*, Boulder, Colorado, 13–14 June 1991. Balkema, Rotterdam, the Netherlands. pp. 531–538.
- Sully, J.P., Robertson, P.K., Campanella, R.G., and Woeller, D.J. 1999. An approach to evaluation of field CPTU dissipation data in overconsolidated fine-grained soils. *Canadian Geotechnical Journal*, **36**(2): 369–381. doi:10.1139/t98-105.
- Taiebat, H.A., and Carter, J.P. 2008. Flow rule effects in the Tresca model. *Computers and Geotechnics*, **35**: 500–503. doi:10.1016/j.compgeo.2007.06.012.
- Vermeer, P.A., and Verruijt, A. 1981. An accuracy condition for consolidation by finite elements. *International Journal for Numerical and Analytical Methods in Geomechanics*, **5**(1): 1–14. doi:10.1002/nag.1610050103.
- Wang, D., White, D.J., and Randolph, M.F. 2010. Large-deformation finite element analysis of pipe penetration and large-amplitude lateral displacement. *Canadian Geotechnical Journal*, **47**(8): 842–856. doi:10.1139/T09-147.
- Westgate, Z.J., White, D.J., and Randolph, M.F. 2012. Field observations of as-laid pipeline embedment in carbonate sediments. *Géotechnique*, **62**(9): 787–798. doi:10.1680/geot.12.OG.001.
- Westgate, Z.J., White, D.J., and Savazzi, M. 2018. Experience with interface shear box testing for axial pipe-soil interaction assessment on soft clay. In *Proceedings of the Offshore Technology Conference*. Paper OTC-28671-MS.
- White, D.J., Gaudin, C., Boylan, N., and Zhou, H. 2010a. Interpretation of T-bar penetrometer tests at shallow embedment and in very soft soils. *Canadian Geotechnical Journal*, **47**(2): 218–229. doi:10.1139/T09-096.
- White, D.J., Hill, A.J., Westgate, Z.J., and Ballard, J.-C. 2010b. Observations of pipe-soil response from the first deep water deployment of the SMARTPIPE. In *Frontiers in Offshore Geotechnics II*. Edited by S. Gourvenec and D. White. pp. 851–856.
- White, D.J., Clukey, E.C., Randolph, M.F., Boylan, N.P., Bransby, M.F., Zakeri, A., et al. 2017. The state of knowledge of pipe-soil interaction for on-bottom pipeline design. In *Proceedings of the Offshore Technology Conference*. OTC 27623.
- Wood, D.M. 1990. Soil behaviour and critical state soil mechanics. Cambridge University Press.
- Yan, Y., White, D.J., and Randolph, M.F. 2011a. Penetration resistance and stiffness factors for hemispherical and toroidal penetrometers in uniform clay. *International Journal of Geomechanics*, **11**(4): 263–275. doi:10.1061/(ASCE)GM.1943-5622.0000096.
- Yan, Y., White, D.J., and Randolph, M.F. 2011b. Investigations into novel shallow penetrometers for fine-grained soils. In *Frontiers in Offshore Geotechnics II*. Edited by S. Gourvenec and D. White. pp. 321–326.
- Yan, Y., White, D.J., and Randolph, M.F. 2017. Elastoplastic consolidation solutions for scaling from shallow penetrometers to pipelines. *Canadian Geotechnical Journal*, **54**(6): 881–895. doi:10.1139/cgj-2016-0286.
- Zienkiewicz, O.C., and Zhu, J.Z. 1992. The superconvergent patch recovery and a posteriori error estimates. Part 1: The recovery technique. *International Journal for Numerical Methods in Engineering*, **33**(7): 1331–1364. doi:10.1002/nme.1620330702.

List of symbols

A_{nom}	nominal area	$s_{\text{u,m}}$	undrained shear strength at mudline
c_h	operative coefficient of consolidation	$s_{\text{u,rem}}$	remoulded undrained shear strength
c_v	coefficient of consolidation	T	mobilized torque
c_{v0}	initial coefficient of consolidation at penetrometer invert	T_{dis}	dimensionless time (dissipation stage)
$c_{v0,\text{LDFF}}$	initial coefficient of consolidation at penetrometer invert derived from LDFF analysis	$T_{\text{dis},50}$	dimensionless time at ~50% consolidation
D	device diameter	$T_{\text{dis},50,\text{ave}}$	dimensionless time at ~50% consolidation (periphery dissipation)
D_{Tbar}	diameter of T-bar penetrometer	t_{dis}	dissipation time
e_0	initial void ratio	u	pore-water pressure
e_{cs}	void ratio on critical state line at $p' = 1$ kPa	V	vertical penetration resistance
f_b	soil buoyancy factor	V_b	resistance due to soil buoyancy
K_0	coefficient of earth pressure at rest	V_{geot}	geotechnical resistance
k	soil permeability	V_{max}	bearing capacity load (end of penetration stage)
k_{su}	gradient of undrained strength profile	V_{pen}	dimensionless velocity (penetration stage)
L	lever arm (toroid penetrometer)	V_s	embedded penetrometer volume (relative to original mudline)
M	slope of critical state line in q - q' space	v_{pen}	vertical penetration speed
m	fitting parameter (dissipation solution)	w	embedment depth
m_{ave}	fitting parameter (periphery consolidation solution)	γ'	effective unit weight
m_v	coefficient of volume compressibility	γ_w	unit weight of water
N	cycle number (cyclic remoulding test)	Δu	excess pore-water pressure
N_b	bearing capacity factor for ball penetrometer	Δu_{ave}	average excess pore-water pressure of different transducer readings
$N_{\text{c,nom}}$	bearing capacity factor	Δu_{ini}	initial excess pore-water pressure at consolidation start
N_t	bearing capacity factor for T-bar	δ	drained interface friction angle
OCR	overconsolidation ratio	θ	local inclination regarding vertical
p'	mean effective stress	κ	slope of elastic compression line
p'_0	initial mean effective stress	λ	slope of virgin compression line
q	penetration resistance	ν	Poisson's ratio
q_0	surcharge at mudline	σ'_n	normal effective stress
R_a	average surface roughness	σ'_{v0}	vertical effective stress
S_t	soil sensitivity	τ_u	undrained shear stress
s_u	undrained shear strength	ϕ'	angle of internal friction
s_{u0}	undrained shear strength at penetrometer invert	ϕ'_{cv}	constant volume friction angle
$s_{\text{u,avg}}$	average undrained shear strength	ψ	drainage index
$s_{\text{u,c}}$	consolidated undrained shear strength		
$s_{\text{u,int}}$	undrained shear strength on interface		